CFD-DEM modelling of particle ejection by a sensor-based automated sorter

Corresponding Author
Robert S Fitzpatrick
Camborne School of Mines, School of Engineering, Mathematics and Physical Sciences, University of Exeter, Penryn Campus, Penryn, UK, TR10 9FE, tel: +44(0)7795 251 704
r.s.fitzpatrick@ex.ac.uk

Co-Authors
Hylke J Glass
Camborne School of Mines, School of Engineering, Mathematics and Physical Sciences, University of Exeter, Penryn Campus, Penryn, UK, TR10 9FE
Richard D Pascoe
Camborne School of Mines, School of Engineering, Mathematics and Physical Sciences, University of Exeter, Penryn Campus, Penryn, UK, TR10 9FE

Abstract

The efficiency of sensor-based automated sorting depends on both correct identification and separation of different types of particles. It is known that the distribution of particles fed to the sorter will affect both of these. When different particles are in close proximity, they can be “agglomerated” or seen as a single particle during identification and also have an increased probability of being unintentionally co-ejected. Both factors will have a negative effect on separation efficiency.

The aim of this work was to model the air ejection manifold of a sensor-based automated sorter and to investigate the relationship between particle proximity and unintentional co-ejections. The airflow from a single air ejection valve of a sorter was modelled using computational fluid dynamics (CFD) software and calibrated against a Tomra Sorting Solutions optical sorter. It was found that the air ejection manifold could be accurately represented in CFD code. Particles were modelled using the discrete element method (DEM) software and the effect of particle position, relative to an air ejection valve, on accurate ejection was examined using an integrated CFD-DEM model. The results of these models matched reasonably well with physical measurements. The models created can be used as a basis for the prediction of sorter efficiency.

Key Words

Sensor-based automated ore sorting; Computational fluid dynamics; discrete element method; solid-fluid system modelling.

1 Introduction

Sensor-based automated sorters are machines which interpret data collected using one or more sensors to classify and separate an input stream of mixed particles. Generally separation is undertaken on a particle-by-particle basis using some external force such as jets of water or compressed air. Sorters have been used in the minerals industry for over 100 years (Manouchehri, 2003) but advances in technology over the last twenty years have led to the proliferation of high-throughput and high-efficiency sorters for mineral processing and a wide range of sensors have been developed.

Most sensors used in automated sorters measure differences in the absorption and/or emission of electro-magnetic radiation. For example, sorters equipped with optical sensors analyse differences in the absorption of radiation in the visible region of the electromagnetic spectrum (390 nm to 790 nm) and have been used to concentrate platinum, coal, magnesite, quartz, base metal sulphides, wolframite, gold, talc and gemstones (Salter and Wyatt, 1991); (Sivamohan and Forssberg, 1991); (Bergmann, 2009).

Sorters are mainly used as a pre-concentration technique to remove barren gangue minerals. They separate material at a coarse grind size and so have the potential to drastically reduce the volume of material which requires further processing. This can greatly improve the energy efficiency of mining by reducing the amount of energy required for comminution. By some estimates, this accounts for up to 75% of the energy consumed on a mine site (Tromans, 2008) and for 3-4% of all energy consumed in the world (Pokrajcic and Lewis-Gray, 2010). Further benefits include the potential to reduce both transport costs and downstream water consumption.

For future implementation of sensor-based automated sorters, the performance in a mineral processing operation should be accurately predicted. A number of factors including feed preparation and sorter set-up and maintenance are known to play a key role in performance (Manouchehri, 2003). The throughput of a sorter will also have a dramatic effect on sorting efficiency (Pascoe et al., 2010). Hence, models relating separation efficiency with throughput are important.

The throughput of a sorter is limited by the requirement to present particles to sensors individually and in a stable position for accurate identification, classification and separation. The feed must therefore be in a monolayer and well separated to ensure a high separation efficiency. The theoretical maximum throughput of sorters with a monolayer feed was investigated for different particle size by De Jong and Harbeck (2005). The authors noted that this maximum was unlikely to be reached due to non-random feed presentation and the requirement of a minimum distance to neighbouring particles. It has been shown that if this minimum distance, or proximity, is below a certain threshold level the efficiency of separation can decreased dramatically. Pascoe et al. (2010) examined the relationship between throughput and separation efficiency for a sorter utilising compressed air jets to separate particles. This work used empirical relationships between a measure of particle proximity, belt loading and separation efficiency to predict sorter performance.

Particle proximity affects the separation efficiency of sorters in two ways. Firstly, when particles are in contact they are incorrectly identified as a single, agglomerated particle and can be misclassified. Secondly, when two or more particles are in close proximity and one is ejected using an external force, the other particles will also be deflected. If the force on the other particles is large enough and there is sufficient exchange of momentum, then the particle will be unintentionally ejected. In this second scenario, it is the proximity of the other particles to the source of the external force rather than the proximity to the particle which is of prime importance.

The focus of the current research was on the second scenario described above. The ejection of particles by a sorter was achieved using jets of compressed air. Valves on the sorter release short bursts of high-pressure, high-velocity air which impinge on particles with sufficient force to change their direction of motion during free flight. The objective of the work

was to investigate the relationship between particle distance to the air jets and the accuracy of the ejection process. This could be used to inform models for the prediction of separation efficiency with changes in throughput. The work consisted of two phases.

In the first phase, a computational fluid dynamics (CFD) model was used to simulate the air released by the compressed air manifold. In the second phase, the calibrated model was combined with a discrete element method (DEM) model to simulate the fluid-solid interactions involved in the ejection of particles by jets of air.

In the second phase, a CFD-DEM model was considered appropriate as previous research has shown that such models have the ability to replicate complex interaction between fluids and moving particles. For example, Chu and Yu (2008) used CFD-DEM models to simulate a number of complex flows including pneumatic conveying and fluidized beds and Wu et al. (2010) modelled gas-solid interactions in catalytic cracking processes. Generally, CFD-DEM work has focussed on densely populated particle-fluid streams containing fine particles. No application of the technique to dilute particulate streams and interactions with large particles was found. To ensure that the models created in the current research were suitable for existing applications, they were validated against experimental data collected using a production scale sensor-based automated sorter.

2 Material and Methods

2.1 Experimental Set-up

The sorter used for the current research was a Tomra Mining Solutions Combi-Sense model BSM063. The sorter utilises a 550 mm wide belt conveyor to accelerate particles to 3 $m \cdot s^{-1}$ for examination. The acceleration of particles decreases relative proximity and supports stabilisation. Examination is undertaken by a 2048-bit line-scan camera and an inductive coil sensor system. The sensors collect data of individual particles which are analysed by a CPU to categorise and classify each particle. Classified particles are physically separated into two product streams whilst in free flight upon leaving the conveyor belt. The primary stream consists of particles which follow a parabolic path described by Newtonian equations of motion. A secondary stream, separated from the primary by a dividing plate, is created by ejecting particles from the primary stream using an array of 128 compressed air valves aligned perpendicular to the belt. When activated, the valves produce jets of high velocity air which create sufficient force to affect the motion of particles and re-direct them into the secondary product stream (Figure 1). The inlet pressure to the air valve manifold was set at 700kPa (gauge).

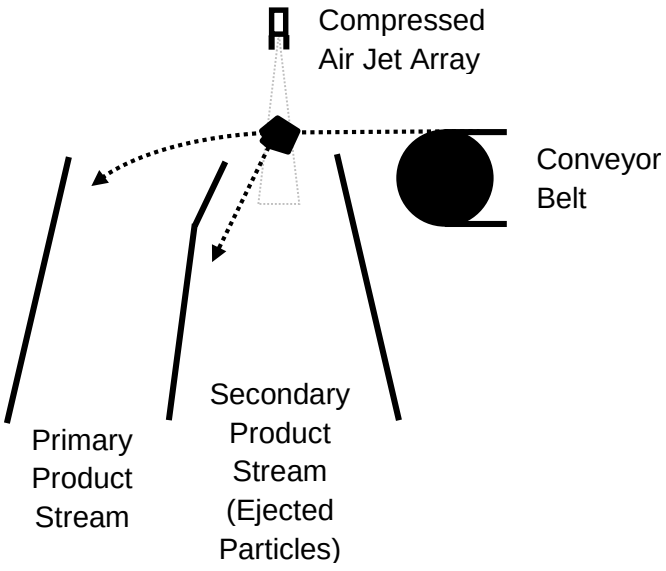

(1 column)

Figure 1 Ejection mechanism of Tomra Mining Solutions Combi-Sense model BSM063

To validate the CFD models used to replicate the fluid flow within a jet of air, temporal and spatial profiles of total pressure during a physical air blast were recorded. These were created by taking measurements of total gauge pressure of the air flow within a jet of air at multiple positions. The data were collected using a 'Transducers Direct' model TD1000 pressure transducer with an inlet diameter of 2 mm. The transducer produced a 0-10V output signal with a response time of less than 1 ms. A PicoTech PicoScope 4000 Series oscilloscope connected to a PC was used to record the data and convert the output to an equivalent total pressure.

The aim of the CFD-DEM modelling was to replicate the area around an air jet in which particles are ejected and to accurately simulate the influence of particle size and shape on this area. To validate the CFD-DEM models, data were collected on the physical ejection of hexahedral particles. Table 1 summarises the dimensions of these particles.

Table 1 Dimensions of test particles used in physical test work

Length and Width, mm	**Height, mm**	**Aspect Ratio (Height / Length)**	**Particle Class Label**
10	10	1	10 mm Cubic
	5	0.5	10 mm Flat
20	20	1	20 mm Cubic
	10	0.5	20 mm Flat

2.2 Numerical Method

Computational modelling was undertaken using the open source software packages Liggghts (www.cfdem.com) and OpenFOAM (www.openfoam.com) for DEM and CFD, respectively. Fluid-particle interactions were modelled using the CFDEMcoupling framework (www.cfdem.com).

The fluid domain was spatially discretised using the finite volume method with values stored at cell centres using the co-located method. The jets of air produced by the sorter were modelled as axisymmetric jets ejecting into quiescent air. Accurate modelling of the air ejection process is complex due to the high pressure changes involved during the process. The ejected air is initially trans-sonic and compressible but, within the domain of interest, it slows down to sub-sonic, essentially incompressible, speeds. A segregated, transient solver based on the Pressure Implicit with Split Operative (PISO) method (Issa, 1986) was used to solve the discretised governing equation within the flow domain. Both compressible and incompressible models were examined.

Testing was divided into two stages. In the first, CFD models were created in two and three dimensional space to simulate the jets of pressurised air created by the sorter. These were validated against experimental data. In the second stage, a three-dimensional CFD-DEM model was used to simulate particle ejection and to test the effects of size, shape and proximity to the air jet on the ejection of particles.

2.2.1 Fluid Phase

For accurate prediction of particle ejection by air jets, it was vital to obtain an accurate representation of the flow of air within the jet stream. The model needed to reproduce accurately both the spatial and temporal profiles of the air flow. To complete this work the fluid phase was modelled using modified versions of Reynolds Averaged Navier-Stokes equations. For incompressible flow, fluid flow was calculated by solving the equations for conservation of mass and momentum (Eq. (1) and Eq. (2)) with suitable boundary conditions. For compressible flow the energy equation was also utilised (Eq. (3)).

$$\frac{\partial \varepsilon_f \rho_f}{\partial t} + \nabla \cdot \varepsilon_f \rho_f U = 0 \quad (1)$$

$$\frac{\partial \varepsilon_f \rho_f U}{\partial t} + \nabla \cdot \varepsilon_f \rho_f UU = -\nabla p - R_{pf} + \nabla \cdot \varepsilon_f \tau + \varepsilon_f \rho_f g \quad (2)$$

$$\frac{\partial \varepsilon_f \rho e}{\partial t} + \nabla \cdot \varepsilon_f \rho eU = -\nabla \cdot \varepsilon_f pU + \nabla \cdot \varepsilon_f \alpha \nabla e \quad (3)$$

Where ε_f, ρ_f, p, e and U are the fluid volume fraction, density, pressure, internal energy and velocity. The fluid stress tensor and the thermal diffusivity are represented by τ and α, whilst g is the gravitational force and R_{fp} is the momentum exchange between fluid and particle phases due to forces exerted by the fluid on all particles within a control volume. The method was described by Goniva et al. (2010) and is based on the work of Gidaspow et al. (1991).

2.2.2 Particle Phase

The motion of discrete particles in the solid phase was modelled by solving Newton's second law of motion (Eq. (4) and Eq. (5)) using the discrete element method originally proposed by Cundall and Strack (1979).

$$m_i \frac{dV_i}{dt} = \sum_{j=1}^{n} \left(F_{c,ij} + F_{d,ij}\right) + m_i g + f_{f,i} \quad (4)$$

$$I_i \frac{d\omega_i}{dt} = \sum_{j=1}^{n} T_{ij} \quad (5)$$

Where m_i, V_i, I_i and ω_i are the particle mass, translational velocity, moment of inertia and rotational velocity. Forces acting on the particles are $f_{c,ij}$, $f_{d,ij}$ and T_{ij} which are the inter-particle contact force, viscous damping force and torque between particle i and n other particles. The force exerted on particle i by the fluid phase is represented by $f_{f,i}$.

A soft-sphere approach was adopted for the calculation of contact and damping forces ($f_{c,ij}$ and $f_{d,ij}$). A modified Hertz-Mindlin non-linear model was used to determine normal and tangential forces resulting from particle contact as described by Johnson (1985) and Mindlin (1949) respectively. The model included terms for particle history and tangential damping. Table 2 summarises the material properties for the particles modelled.

Table 2 Summary of material properties in discrete element modelling

Material Property	**Value**
Young's modulus	5 x 10^6 Pa
Poisson's ratio	0.45
Coefficient of restitution	0.3
Coefficient of friction	0.5
Density	2.7 x 10^3 kgm^{-3}

2.2.3 Particle-Fluid Interactions

Particle-fluid interactions were modelled using a resolved CFD-DEM method with full two-way coupling between fluid and particle phases. The particle-fluid interaction forces considered were the pressure gradient, buoyancy and the fluid drag, as modelled by Di Felice (1994). The model A approach (Zhou et al., 2010) best corresponds to the current scenario where the flow regime is unsteady and non-uniform and is hence adopted as the most appropriate model.

2.2.4 Computational Domains

Simulations were undertaken on two and three dimensional grids. The two dimensional grid was used initially to find suitable input variables, these were translated to a three dimensional grid for further optimisation.

2.2.4.1 Two Dimensional Domain

Figure 2 shows a schematic diagram of the region modelled in two dimensions during the initial CFD testing.

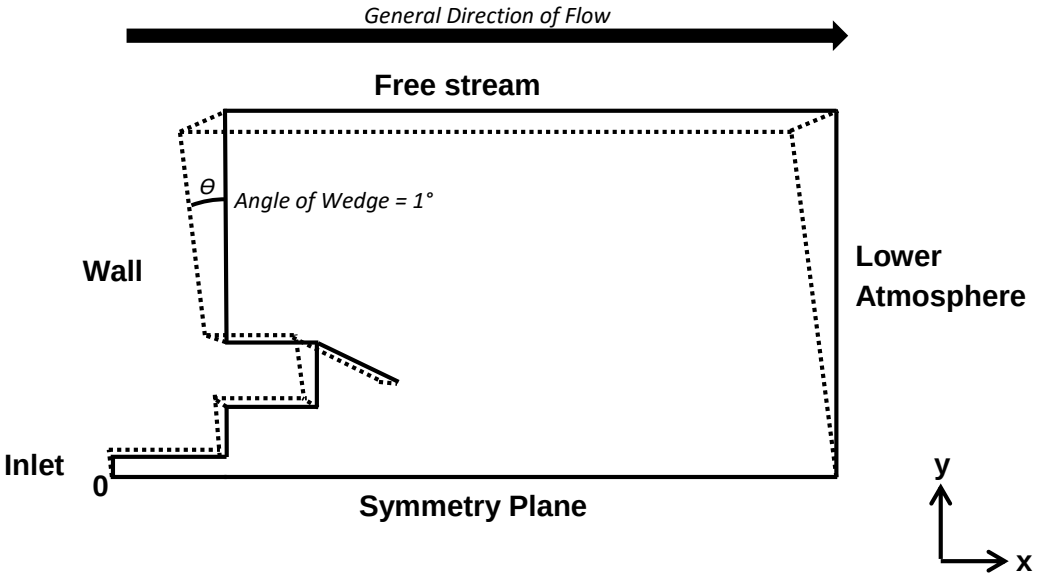

(2 columns)

Figure 2 Schematic of two-dimensional wedge shaped domain modelled using CFD

The primary axis (x) of the two-dimensional model was defined as parallel to the centre line of the air jet. The origin was set at the intersection of the centreline and the inlet boundary. A computational grid was created based on this schematic.

Five boundaries were defined for the computational domain. The name and mathematical behaviour at each boundary is summarised in Table 3. The behaviour at some boundaries varied to suit incompressible or compressible models, e.g. a wave transmissive boundary was defined for the outlet during compressible modelling and a zero gradient boundary for incompressible flow. The inlet air pressure and velocity were varied with time to simulate the finite time required for the opening and closing of the valve and the resulting temporal profile of the jet of air.

Table 3 Summary of boundary condition and behaviour in CFD modelling

Boundary	**Description**	**Defining properties**
Inlet	Inlet for high pressure air	Time varying Total Pressure or Velocity
Lower Atmosphere	Quiescent air parallel to the inlet	Wave transmissive or zero gradient
Wall	Physical boundaries of valve and sorter	No slip boundary conditions
Free stream	Quiescent air perpendicular to the inlet	Pressure fixed at 100kPa
Symmetry Plane	Central axis of the airstream	Disregarded during computation

2.2.4.2 Three Dimensional Domain

Figure 3 shows a schematic diagram of the region modelled in three dimensions for further CFD testing and for CFD-DEM testing.

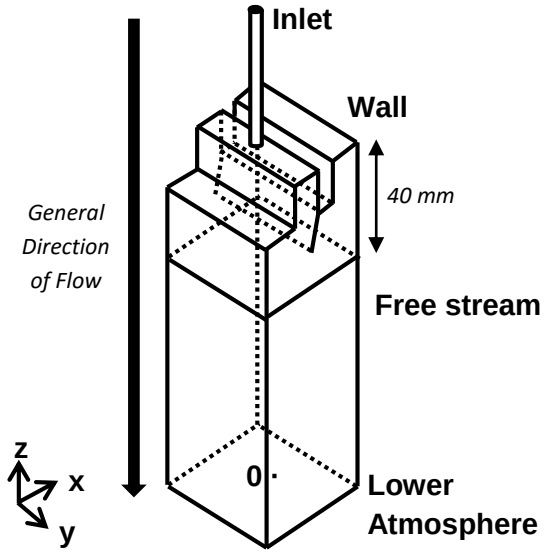

(1 column)

Figure 3 Schematic of three-dimensional domain used for CFD-DEM modelling

For the three-dimensional modelling, the primary axis (x) was defined as parallel to the horizontal direction of travel of particles. The secondary axis (y) was set perpendicular to this in the same horizontal plane. The tertiary axis (z) was defined as vertical. The origin was set at the intersection of the axisymmetric centre of the jet of air and the 'lower atmosphere' boundary. The boundary conditions used for the three-dimensional CFD-DEM simulations were the same as the conditions from the two-dimensional CFD simulations. To reduce computational expense, the air jet was assumed to be axisymmetric and obtained from CFD modelling of a quarter of the domain shown in the schematic diagram. This was mirrored and used to create the CFD-DEM model domain. The CFD-DEM model covered the entire domain in the x-y plane and in the z axis started 40 mm from the air jet (approximate position marked in schematic diagram).

2.2.4.3 Computational Grid Resolution

The three dimensional CFD grid contained 216458 cells. The grid was graded so that the highest resolution was in the area of greatest fluid velocity. The average cell volume in these areas was 0.9 mm^3. The overall average cell volume was 1.8 mm^3 with a minimum volume of 0.012 mm^3 and maximum of 3.5 mm^3. Figure 4 shows the grid resolution at a distance of 75 mm from the air jet, which is the approximate distance at which the fluid-particle interactions occurred.

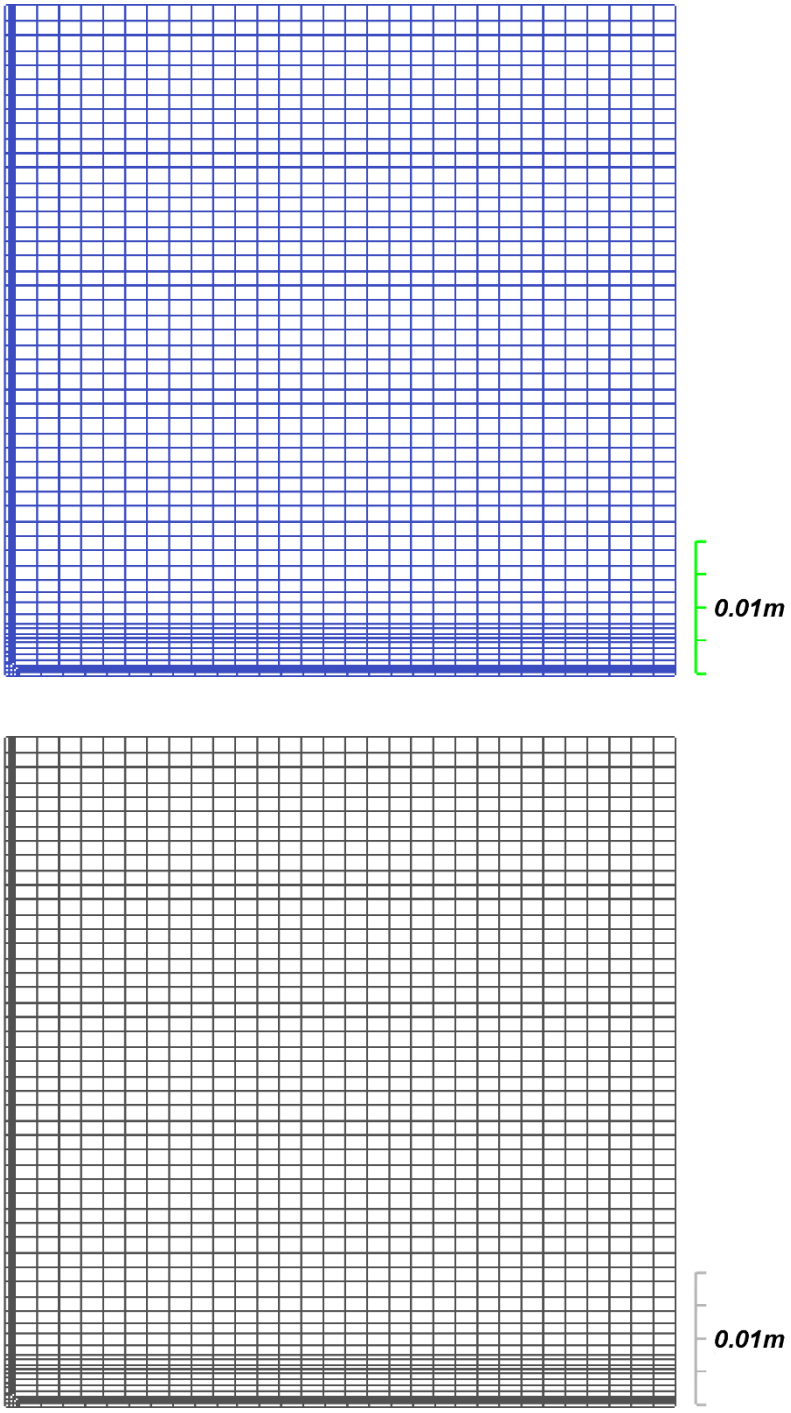

Figure 4 Cross-section of CFD grid (x-y) at a distance of 75mm (z) from the air inlet valve

The CFD-DEM grid contained 571200 cells. The average cell size was approximately 1mm^3 with a minimum volume of 0.03 mm^3 and maximum of 1.85 mm^3.

The grid resolution was chosen as a compromise between accurately modelling the process and ensuring the simulations were stable and solvable in a practical time frame. Over 500 simulations were run to determine the area of influence of the air jet. Simulations were run on a high spec computer with eight-core processor with each CFD-DEM simulation requiring approximately 6.5 hours for completion whilst maintaining a maximum Courant number of 1-1.5.

The Courant number, or Courant-Friedrichs-Lewy criterion, provides a measure connecting the fluid velocity, time step and cell dimensions to ensure that partial differential equations converge, see Eq. (6).

$$C = \frac{U\Delta t}{\Delta x} \tag{6}$$

Where C, U, Δt and Δx are the Courant number, fluid velocity, time step and cell length respectively. Tests at twice the resolution were estimated to take approximately 100-200 hours to complete in order to ensure that the Courant number remained at a stable level.

2.2.5 CFD-DEM Coupling

Particles were created for the CFD-DEM modelling with properties which matched those used during physical testing. A multi-sphere method was used to create representations of the physical particles. It was found that 27 spheres were sufficient to model cubic particles and 9 spheres sufficient to model flat particles. The diameter of each sphere was either 5mm or 10mm. These were chosen as the resolved CFD-DEM approach adopted requires that the particle diameters are eight times the size of the grid diameter to obtain mesh independent results (Hager, 2014).

The general approach to the CFD-DEM coupling was to set the horizontal position and velocity of particles in relation to the centreline of the jet of air. The velocity of the particle was set to 3 $m \cdot s^{-1}$ in the primary axis (v_x) and to 0 $m \cdot s^{-1}$ in the secondary (v_y). The vertical components of position (x_z) and velocity (v_z) were calculated based on the distance travelled on leaving the conveyor belt, ignoring air resistance of the quiescent air.

The area of influence for an air jet was determined by varying the position of particles relative to the origin. The interaction between CFD and DEM forces were simulated within the domain of interest (see Figure 5) and the particles were tracked to the point of separation at the dividing plate between primary and secondary streams (see Figure 6).

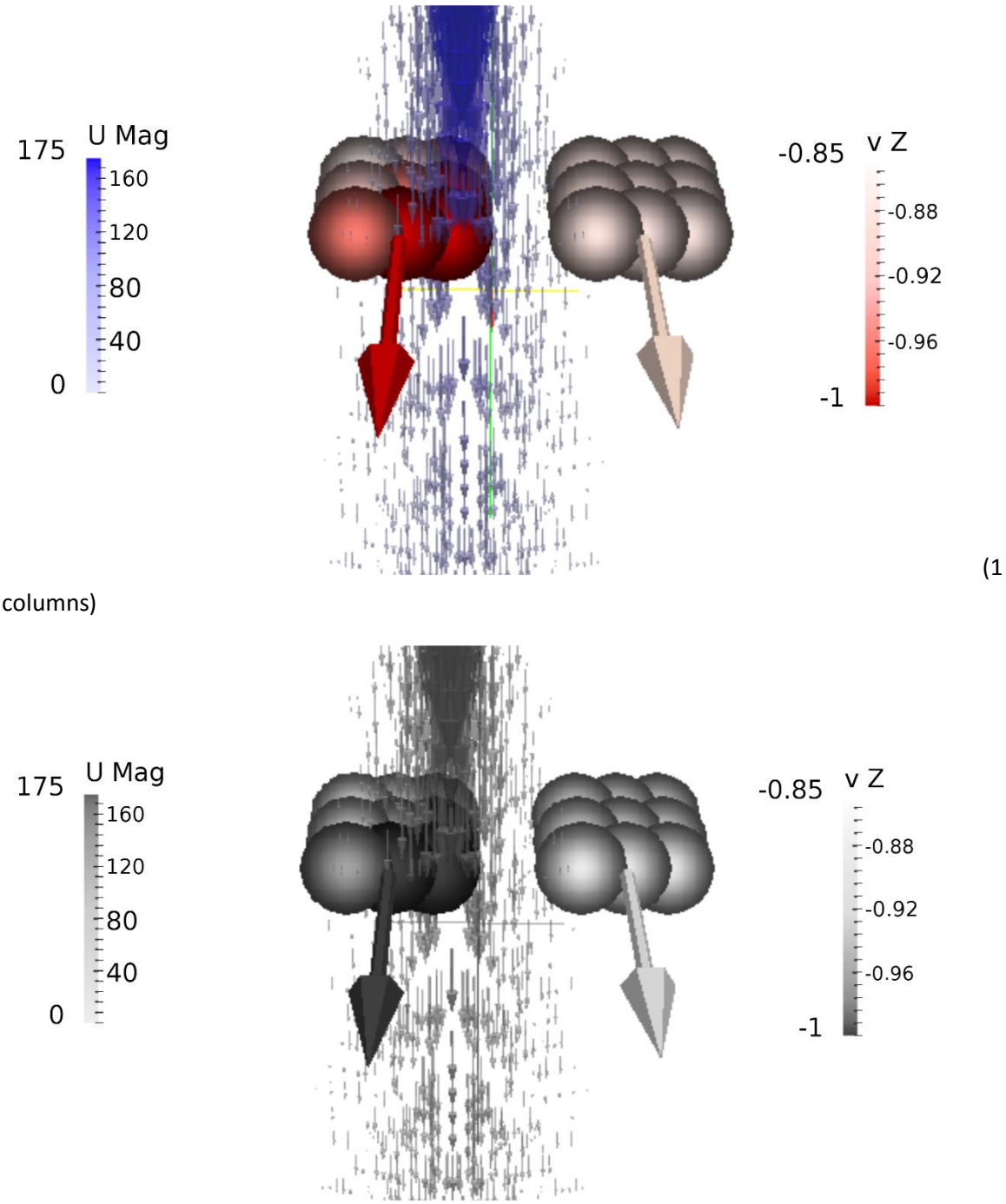

(1 columns)

Figure 5 Example of fluid-particle interaction showing effect of particle distance to axisymmetric jet centre. ‘U Mag’ is the magnitude of the velocity of air and ‘vZ’ is the vertical component of the particle velocity. Arrows show the direction of particle motion

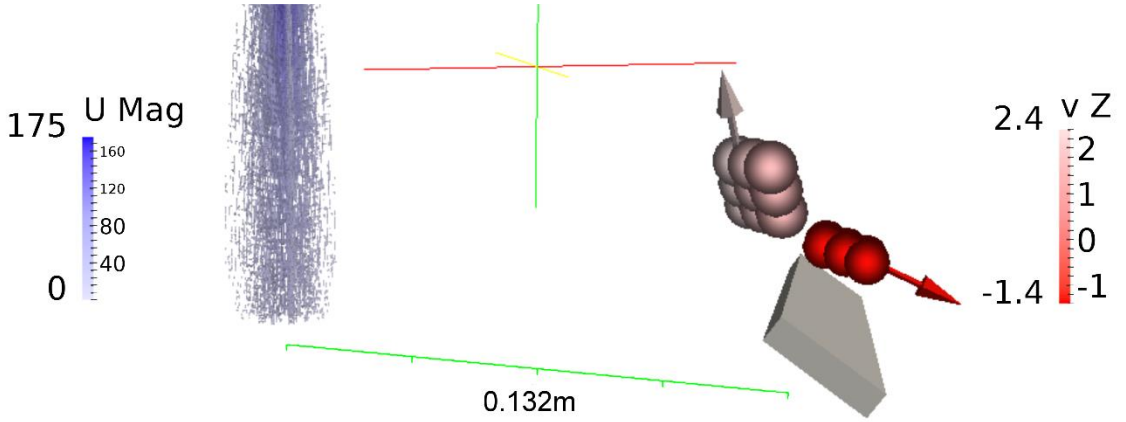

(2 columns)

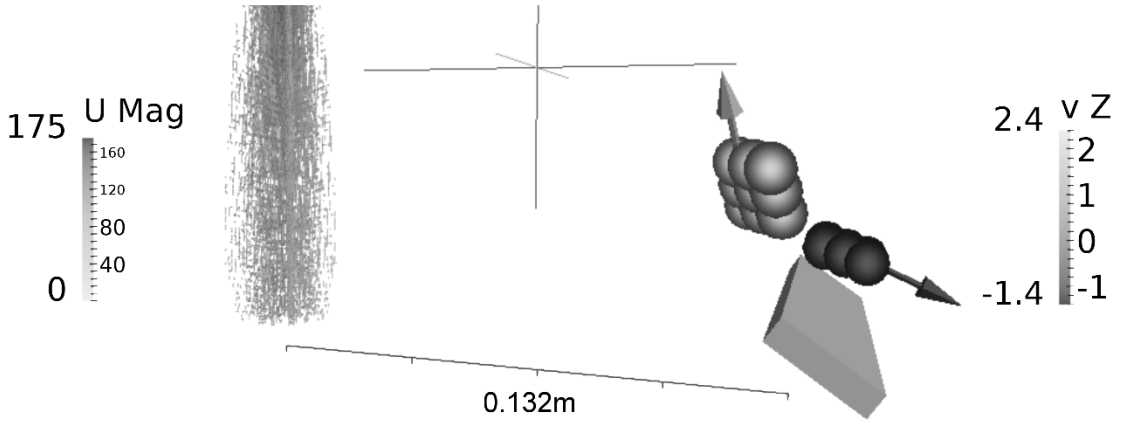

Figure 6 Example of particle separation by splitter bar after fluid-particle interaction. 'U Mag' is the magnitude of the velocity of air and 'vZ' is the vertical component of the particle velocity, the scale line has units of metres

3 Results and Discussion

3.1 CFD Model of Jets of Air

CFD simulations of a valve releasing compressed air were undertaken initially on the two-dimensional mesh, these results were then used to optimise a three dimensional grid. To optimise the results solvers for compressible fluids were tested with pressures varying from 400 kPa to 900 kPa. Solvers for incompressible fluids were also tested with inlet velocities ranging from 600 $m \cdot s^{-1}$ to 900 $m \cdot s^{-1}$. From these simulations, profiles of the relative total gauge pressure along the centreline of the jet were validated against experimental results from the pressure transducer. It was found that compressible simulations with an inlet pressure of 700 kPa matched the experimental results well. For the incompressible model, an inlet velocity of 880 $m \cdot s^{-1}$ produced the best match to the experimental results. Figure 7

contains a chart of a profile along the centreline of the jet of air. It shows the optimised simulation results and experimental data.

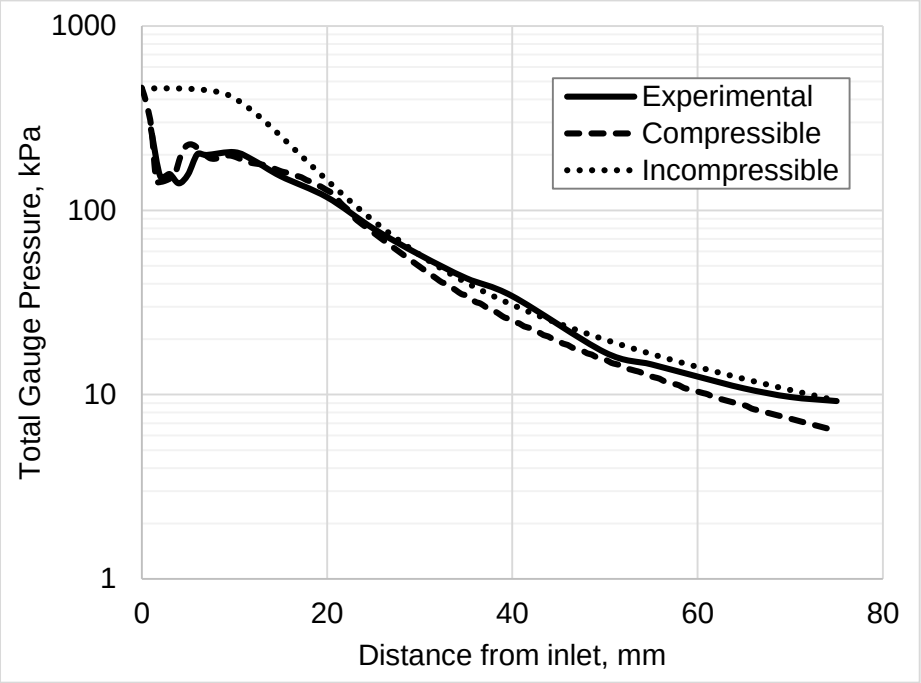

(2 columns)

Figure 7 Pressure decay along axisymmetric jet, gauge pressure relative to atmosphere (101kPa)

Figure 7 shows that the compressible model agrees well with the experimental results across the entire profile. The simulation preserves the under-expanded transonic nature of the air jet close to the inlet. While the incompressible model does not agree with the experimental data in this region, a better match is achieved further from the inlet. Importantly, it matches well in the region in which the interaction between particles and fluid occurs. The position of the area of interaction was determined using Newton's equations of motion alongside careful measurements of the position of the feed belt and compressed air valve. The path of particles was determined and the distance between compressed air valve and particle at the point of ejection calculated. The estimated results were confirmed using a 1000 frames per second high speed camera.

Figure 8 shows the total gauge pressure, measured perpendicular to the jet, in the region of particle interaction. It can be seen that very good agreement between the simulation results and the experimental data were obtained.

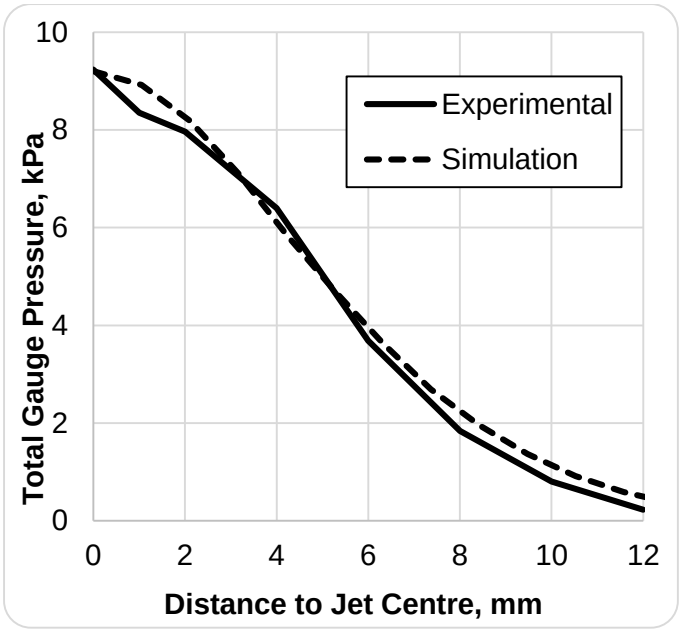

(1 column)

Figure 8 Pressure decay perpendicular to axisymmetric air jet at a distance of 75mm from the inlet, gauge pressure relative to atmosphere (101kPa)

Figure 8 shows that the incompressible model matches the experimental data well in the region of particle-fluid interaction. The compressible model underestimates the total pressure, which is likely a result of over-dispersion by the turbulence model or overly large densities closer to the air inlet.

The figure also shows that the variation in pressure across the profile is about 10 kPa which is less than 10% of atmospheric pressure. The results also suggest that the maximum velocity was about Mach 0.35 and the average was about Mach 0.2. Data from the compressible model estimate that the density varied by less than 5% across this same range.

The above results suggest that an incompressible model is adequate to simulate the air ejection in the region of particle interaction. The generally accepted limit of incompressibility is Mach 0.3, so that the maximum velocity observed here is arguably a little too high. However, the average velocity is much less than this and the density and pressure changes are relatively low. Hence, the incompressible model was chosen for the second phase of work. An advantage to this approach is that the incompressible models are less computationally expensive than their compressible counterparts.

To accurately model the air ejection of the sensor-based automated sorter it was necessary to replicate not only the spatial profile of the jets but also the temporal profile. To validate the CFD models, the total gauge pressure of a jet of air was recorded during 8 ms blasts and an average profile was created. The data were collected within the region of fluid-particle interaction and at the axisymmetric centre of the jet. Figure 9 shows the temporal profile of the air flow and the equivalent results from the incompressible model.

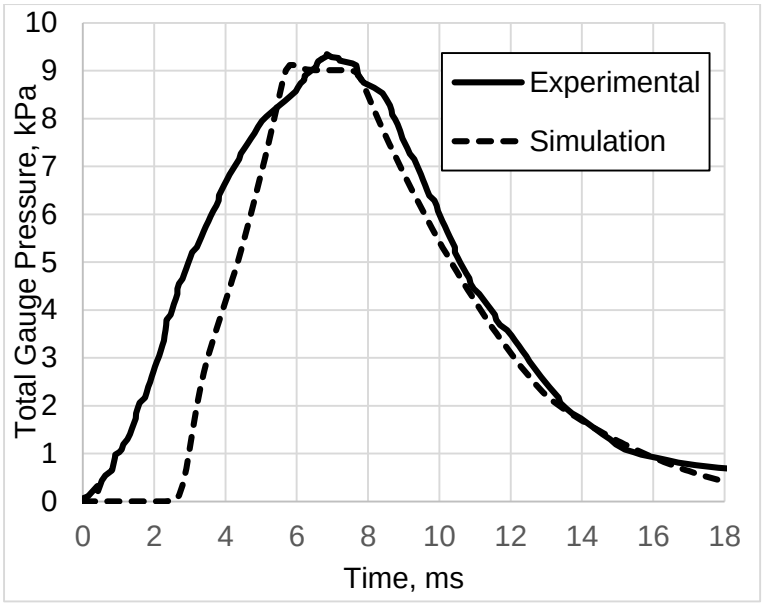

(1 column)

Figure 9 Temporal profile of compressed air blast. Measured on jet centreline at a distance of 75 mm from the inlet

Figure 9 shows that there is generally good agreement between the model and experimental data. The maximum pressures are very similar and reached at approximately the same time (6 ms - 7 ms). The dissipation of pressure after the valve is closed (after 8 ms) is also similar. However, upon opening the valve the pressure observed experimentally in the region of interest begins to increase approximately 2.8 ms before the model predicts.

3.2 CFD-DEM Model of Particle Ejection

The area of influence of an air jet for different particle types was found both experimentally and using CFD-DEM simulations. For experimental data, the boundary of this area was defined by the point at which all particles were missed by the air jet. This was determined to the nearest 0.5 mm along the primary axis and nearest 3 mm along the secondary axis. This variation in resolution was a result of the limiting factors in either direction. For the primary axis, the limit was the length of a pixel which was about 0.3 mm. For the secondary axis, the limit was the minimum change in delay time which was 1 ms, equivalent to about 3 mm.

For the CFD-DEM simulations, the boundary of the area of influence was determined by varying particle position and observing trajectories relative to the dividing plate. A binary reject/accept result was then recorded and the boundary determined by the limit of ejection to the secondary stream. To account for errors in the measurement of the position of the dividing bar relative to the air jet, results were recorded with the plate in different positions determined by the expected margins of error. It was found that there was little change in result over this range. The results were averaged and determined to the nearest 0.5 mm in the primary axis (labelled y in Figure 3) and 3 mm in the secondary axis (labelled x in Figure 3).

It was found both experimentally and using CFD-DEM simulations that all particles except for the 20 mm cubic particles could be ejected by a single air jet. The areas of influence for the remaining particle types are shown in Figure 10, Figure 11 and Figure 12. The position of the origin shown in these figures is based on optimised settings from the experimental data.

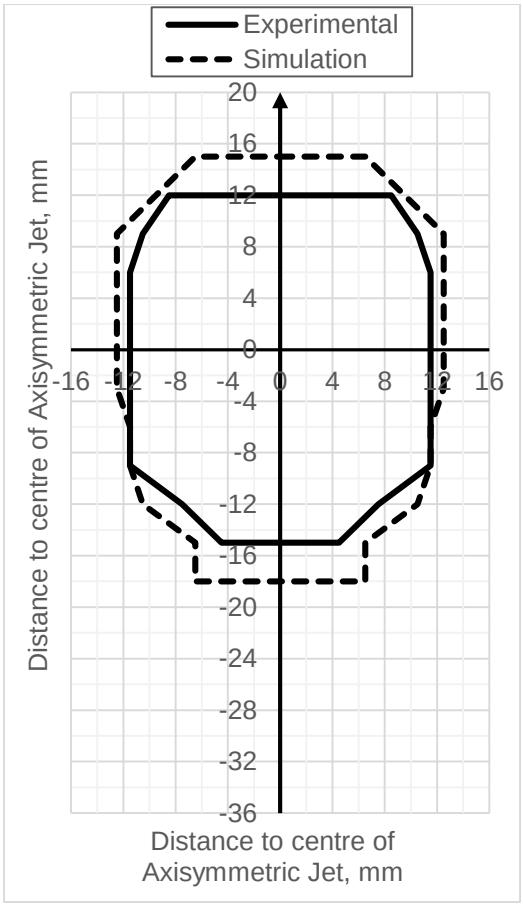

(1.5 column)

Figure 10 Area of influence around axisymmetric jet for ’20 mm Flat’ particles (20 mm x 20 mm x 10 mm with density of 2700 g·cm-3), arrow represents direction of particle motion

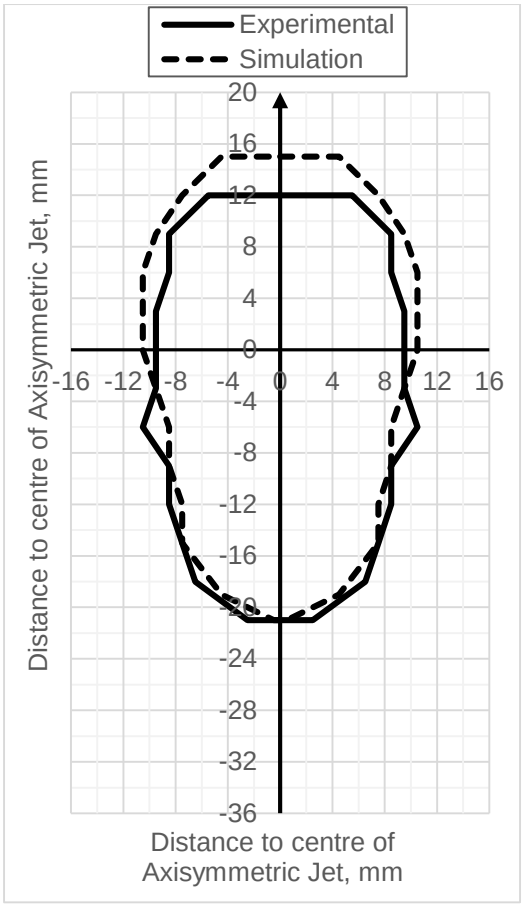

(1.5 column)

Figure 11 Area of influence around axisymmetric jet for ’10 mm Cubic’ particles (10 mm x 10 mm x 10 mm with density of 2700 g·cm-3), arrow represents direction of particle motion

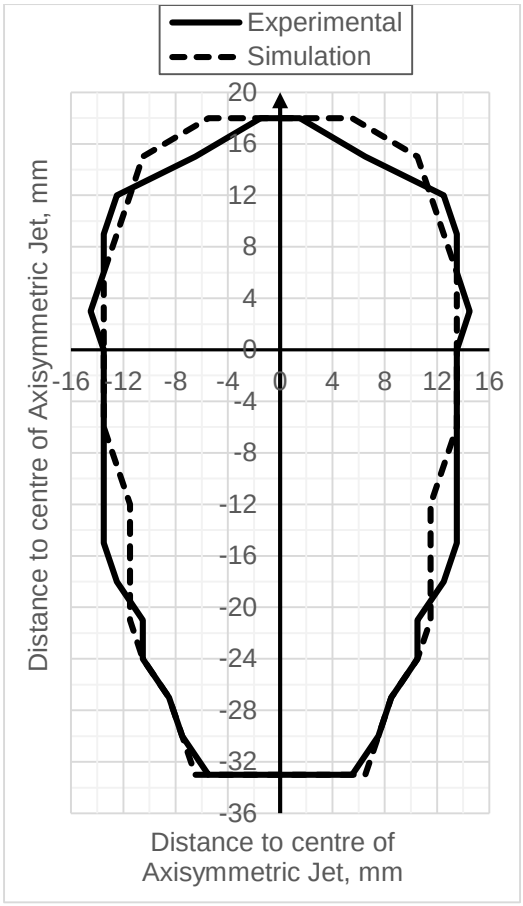

(1.5 column)

Figure 12 Area of influence around axisymmetric jet for ’10 mm Flat’ particles (10 mm x 10 mm x 5 mm with density of 2700 g·cm-3), arrow represents direction of particle motion

It can be seen that there is good agreement between experimental and simulated results with trends between particle types correctly identified. The simulation correctly estimated the length of influence in the primary axis for the ’10 mm Flat’ fraction, whilst overestimating by 3 mm the boundary for particles in front of the origin in the ’10 mm Cubic’ fraction and by 3 mm in both directions for the ’20 mm Flat’ fraction. This difference may have been less if the sorter was not limited to minimum changes in ejection time of 1 ms.

The average error of estimation in the secondary axis was 1.6 mm for the ’10 mm Cubic’ fraction, about 1.1 mm for the ‘10 mm Flat’ fraction and 2.2 mm for the ’20 mm Flat’ fraction. The area of the region of influence for the simulated ’10 mm Flat’ particles was 98% of the actual area. The equivalent values for the ’10 mm Cubic’ and ’20 mm Flat’ were 101% and 129%, respectively. Again, with a more accurate control over the change in ejection time, these values would likely be less.

Most of the errors occur when the distance to the jet in the primary axis is greatest. This result is not surprising when the temporal profile of the air blast is examined over the entire spatial range of influence. For example, Figure 13, Figure 14 and Figure 15 show the temporal profile of the air blast as the distance from the axisymmetric jet increases in the secondary axis. These charts can be compared directly with Figure 9 which shows the blast at the centre of the jet.

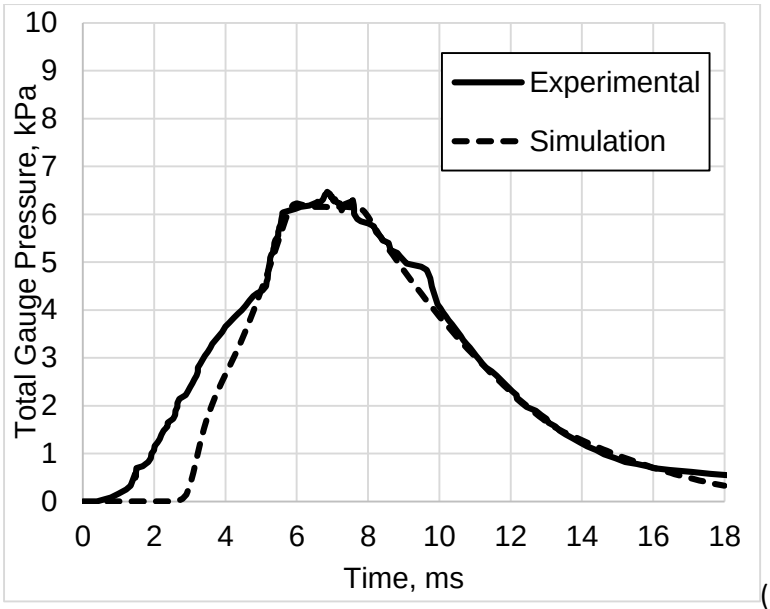

(1 column)

Figure 13 Temporal profile of compressed air blast. Measured 4 mm along the secondary axis at a distance of 75 mm from the inlet

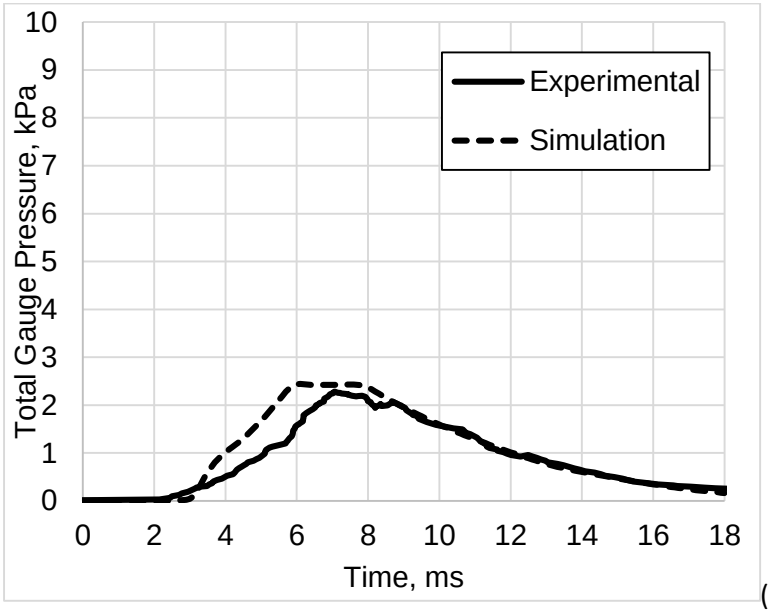

(1 column)

Figure 14 Temporal profile of compressed air blast. Measured 8 mm along the secondary axis at a distance of 75 mm from the inlet

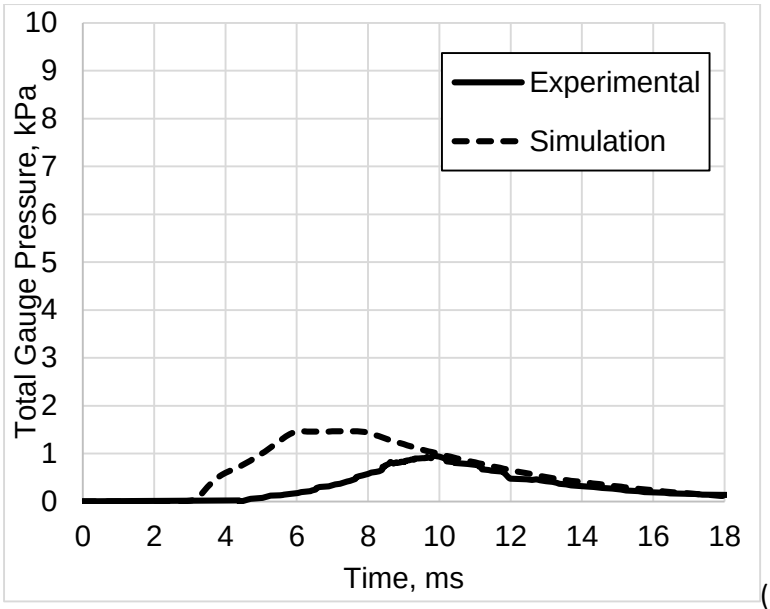

(1 column)

Figure 15 Temporal profile of compressed air blast. Measured 10 mm along the secondary axis at a distance of 75 mm from the inlet

Comparing Figure 9, Figure 13, Figure 14 and Figure 15, it can be seen that as the distance from the centreline of the jet increases in the secondary axis the simulated air pressure diffuses at a lower rate than observed experimentally. This has had the result of overestimating the influence of the jet at greater distances from the jet, especially as the distance from the jet in the primary axis is increased.

A further potential source for the error is the use of large spheres in the model particles. The '20mm Flat' particles produced the worst results and these used larger spheres than the other model particles. This result could also be explained by the errors in the CFD model which would have a greater influence on the larger surface area of the '20 mm Flat' particles.

4 Conclusions

The ejection of particles by a sensor-based automated sorter has been accurately simulated using CFD-DEM. The area around the centreline of a jet, in which particles are ejected, can be accurately predicted. The CFD-DEM model was able to accurately predict the effect of particle size and flakiness on the area of influence associated with an air jet.

The current work provides a solid foundation for predicting the effect of spatial distributions of feed material on sorter performance. The results show that these effects can be evaluated by computer simulations validated by reported results. This is extremely useful to reduce sorter performance test work, which is time-consuming and requires large masses of material.

Further investigations will seek to develop the model using higher grid resolutions. These higher resolutions would allow for more complex modelling of particles using smaller sphere diameters without compromising the integrity of the model and maintaining suitable particle diameter to grid size ratios.

To improve on the simulation of a sorter it is necessary to model the ejection of particles using multiple air-jets. This is essential for the simulation of larger sized particles. For

example, the experimental work undertaken indicated that either multiple air jets or jets at a higher pressure are required to eject 20 mm^3 particles. The interaction of the fluid flows from multiple jets and the consequent effects on particle ejection can be modelled using the techniques outlined in the current research.

The overall goal of this research is to create CFD-DEM simulations of the full sorting process from particle positioning in the feed to ejection. Such a tool could be used to predict the effects of changes to sorter variables on performance.

This includes for example:

- The pressure, spacing and design of air jets
- The particle size range, shape and throughput
- The design of feeders, belts and ejection chambers

Such work is limited by the computational expense of modelling large numbers of particle and fluid interactions but in the future may well be a viable option when predicting sorter performance.

Acknowledgements

The authors would like to acknowledge the work of the OpenFOAM foundation, DCS Computing GmbH and all contributors to the LIGGGHTS, OpenFOAM and CFDEM open source computer codes.

References

Bergmann, C., 2009. Developments in Ore Sorting Technologies, in: Proceedings of Mintek 75: A Celebration of Technology. Presented at the Mintek 75: A Celebration of Technology, Randburg, South Africa.

Chu, K.W., Yu, A.B., 2008. Numerical simulation of complex particle–fluid flows. Powder Technology, WCPT5 Papers presented at the 5th World Conference of Particle Technology (WCPT5), Orlando, Florida, April 23–27 2006 5th World Conference of Particle Technology (WCPT5) 179, 104–114. doi:10.1016/j.powtec.2007.06.017

Cundall, P.A., Strack, O.D.L., 1979. A discrete numerical model for granular assemblies. Géotechnique 29, 47–65. doi:10.1680/geot.1979.29.1.47

De Jong, T.P.R., Harbeck, H., 2005. Automated sorting of minerals: current status and future outlook, in: Proceedings of the 37th Canadian Mineral Processors Conference. Presented at the 37th Canadian Mineral Processors Conference, pp. 629–648.

Di Felice, R., 1994. The voidage function for fluid-particle interaction systems. International Journal of Multiphase Flow 20, 153–159. doi:10.1016/0301-9322(94)90011-6

Gidaspow, D., Bezburuah, R., Ding, J., 1991. Hydrodynamics of Circulating Fluidized Beds: Kinetic Theory Approach (No. CONF-920502-1). Illinois Inst. of Tech., Chicago, IL (United States). Dept. of Chemical Engineering.

Goniva, C., Kloss, C., Hager, A., Pirker, S., 2010. An open source CFD-DEM perspective, in: Proceedings of OpenFOAM Workshop, Göteborg.

Hager, A., 2014. CFD-DEM on Multiple Scales - An Extensive Investigation of Particle-Fluid Interactions. Johannes Kepler University Linz, Linz.

Issa, R.I., 1986. Solution of the Implicitly Discretised Fluid Flow Equations by Operator-splitting. J. Comput. Phys. 62, 40–65. doi:10.1016/0021-9991(86)90099-9

Johnson, K.L., 1985. Contact Mechanics. Cambridge University Press, Cambridge.

Manouchehri, H.-R., 2003. Sorting: Possibilities, Limitations and Future.

Mindlin, R.D., 1949. Compliance of elastic bodies in contact. Journal of Applied Mechanics 16, 259–268.

Pascoe, R.D., Udoudo, O.B., Glass, H.J., 2010. Efficiency of automated sorter performance based on particle proximity information. Minerals Engineering 23, 806–812. doi:10.1016/j.mineng.2010.05.021

Pokrajcic, Z., Lewis-Gray, E., 2010. Advanced Comminution Circuit Design – Essential for Industry. AusIMM Bulletin 38–42.

Salter, J.D., Wyatt, N.P.G., 1991. Sorting in the minerals industry: Past, present and future. Minerals Engineering 4, 779–796. doi:10.1016/0892-6875(91)90065-4

Sivamohan, R., Forssberg, E., 1991. Electronic sorting and other preconcentration methods. Minerals Engineering 4, 797–814. doi:10.1016/0892-6875(91)90066-5

Tromans, D., 2008. Mineral comminution: Energy efficiency considerations. Minerals Engineering 21, 613–620. doi:10.1016/j.mineng.2007.12.003

Wu, C., Cheng, Y., Ding, Y., Jin, Y., 2010. CFD–DEM simulation of gas–solid reacting flows in fluid catalytic cracking (FCC) process. Chemical Engineering Science, 20th International Symposium in Chemical Reaction Engineering—Green Chemical Reaction Engineering for a Sustainable Future 65, 542–549. doi:10.1016/j.ces.2009.06.026

Zhou, Z.Y., Kuang, S.B., Chu, K.W., Yu, A.B., 2010. Discrete particle simulation of particle–fluid flow: model formulations and their applicability. Journal of Fluid Mechanics 661, 482–510. doi:10.1017/S002211201000306X